



Magnetospheric ion sputtering and water ice grain size at Europa

T.A. Cassidy^{a,*}, C.P. Paranicas^b, J.H. Shirley^c, J.B. Dalton III^c, B.D. Teolis^d, R.E. Johnson^e,
L. Kamp^c, A.R. Hendrix^c

^a Laboratory for Atmospheric and Space Physics, University of Colorado Boulder, 1234 Discovery Dr., Boulder, CO 80303, USA

^b Applied Physics Laboratory, Johns Hopkins University, 11100 Johns Hopkins Road, Laurel, MD 20723, USA

^c Jet Propulsion Laboratory, California Institute of Technology, 4800 Oak Grove Road, Pasadena, CA 91109, USA

^d Southwest Research Institute, Space Science and Engineering Division, 6220 Culebra Rd., San Antonio, TX 78238, USA

^e University of Virginia, Charlottesville, VA 22904, USA

ARTICLE INFO

Article history:

Received 24 January 2012

Received in revised form

24 June 2012

Accepted 9 July 2012

Available online 27 July 2012

Keywords:

Europa

Water Ice Sputtering Yields

Galileo NIMS Data Analysis

ABSTRACT

We present the first calculation of Europa's sputtering (ion erosion) rate as a function of position on Europa's surface. We find a global sputtering rate of $2 \times 10^{27} \text{ H}_2\text{O s}^{-1}$, some of which leaves the surface in the form of O_2 and H_2 . The calculated O_2 production rate is $1 \times 10^{26} \text{ O}_2 \text{ s}^{-1}$, H_2 production is twice that value. The total sputtering rate (including all species) peaks at the trailing hemisphere apex and decreases to about 1/3rd of the peak value at the leading hemisphere apex. O_2 and H_2 sputtering, by contrast, is confined almost entirely to the trailing hemisphere. Most sputtering is done by energetic sulfur ions (100s of keV to MeV), but most of the O_2 and H_2 production is done by cold oxygen ions (temperature $\sim 100 \text{ eV}$, total energy $\sim 500 \text{ eV}$). As a part of the sputtering rate calculation we compared experimental sputtering yields with analytic estimates. We found that the experimental data are well approximated by the expressions of Famá et al. for ions with energies less than 100 keV (Famá, M., Shi, J., Baragiola, R.A., 2008. Sputtering of ice by low-energy ions. *Surf. Sci.* 602, 156–161), while the expressions from Johnson et al. fit the data best at higher energies (Johnson, R.E., Burger, M.H., Cassidy, T.A., Leblanc, F., Marconi, M., Smyth, W.H., 2009. Composition and Detection of Europa's Sputter-Induced Atmosphere, in: Pappalardo, R.T., McKinnon, W.B., Khurana, K.K. (Eds.), *Europa*. University of Arizona Press, Tucson.). We compare the calculated sputtering rate with estimates of water ice regolith grain size as estimated from Galileo Near-Infrared Mapping Spectrometer (NIMS) data, and find that they are strongly correlated as previously suggested by Clark et al. (Clark, R.N., Fanale, F.P., Zent, A.P., 1983. Frost grain size metamorphism: Implications for remote sensing of planetary surfaces. *Icarus* 56, 233–245.). The mechanism responsible for the sputtering rate/grain size link is uncertain. We also report a surface composition estimate using NIMS data from an area on the trailing hemisphere apex. We find a high abundance of sulfuric acid hydrate and radiation-resistant hydrated salts along with large water ice regolith grains, all of which are consistent with the high levels of magnetospheric bombardment at the trailing apex.

© 2012 Elsevier Ltd. All rights reserved.

1. Introduction

The Galilean satellites are exposed to intense space weathering by ions and electrons in Jupiter's magnetosphere. This has been invoked to explain large-scale features in the moons' reflectance spectra. The trailing hemisphere, which is upstream with respect to magnetospheric flow, is darker and redder than the leading hemisphere (e.g., Pospieszalska and Johnson, 1989) and has more sulfur compounds owing to the logenic sulfur-rich plasma bombarding the moon (e.g., Hendrix et al., 2011). Relating these

features to magnetospheric bombardment requires the calculation of ion flux as a function of position on the surface.

In this paper we describe calculations of ion flux and sputtering (erosion) rate. Sputtering is a particularly robust process at Europa's surface owing to the bombardment of energetic heavy ions (Cooper et al., 2001). Because sputtering selectively removes smaller regolith grains, we compare our calculated sputtering pattern with grain size as determined by recent analyses of Galileo NIMS (Near Infrared Mapping Spectrometer) data (see companion paper by Dalton et al. (2012)). We find that the calculated sputtering rate is correlated with regolith grain size; large calculated sputtering rates correspond to large grain sizes. We also present, for the first time, surface composition and grain size information for a location near Europa's trailing side apex at 0° , 270°W .

* Corresponding author. Tel.: +1 434 806 9880.

E-mail address: timothy.cassidy@lasp.colorado.edu (T.A. Cassidy).

Pospieszalska and Johnson (1989) made the most recent estimates of the ion bombardment pattern. Since then the Galileo mission has provided new information about Europa's plasma environment (Paranicas et al., 2009; Kivelson et al., 2009). Though they only considered the flux of sulfur ions and did not calculate the sputtering rate, other papers have taken their fluxes as a proxy for sputtering rate (e.g., Tiscareno and Geissler, 2003; Cassidy et al., 2008). We show here that ion flux and sputtering rate are quite distinct.

In this paper we cover a variety of topics with the goal of calculating ion flux maps and sputtering rates. Sputtering an ice surface produces mostly H₂O with a fraction of O₂ and H₂, but the latter are important in that they are the primary suppliers of Europa's atmosphere and neutral gas cloud (or 'torus').

2. Calculation details

2.1. Model description

The model we used to calculate ion flux is similar to Pospieszalska and Johnson (1989), we 'trace' ion trajectories as they gyrate around Jupiter's magnetic field lines and 'drift' relative to Europa. The ion motion is treated as a superposition of three motions (see Fig. 1): (1) A circular motion perpendicular to the magnetic field line with a radius called the gyroradius and speed given by $v\sin(\alpha)$, where v is the ion speed and α is called the pitch angle, the angle of the ion's velocity relative to the field line. (2) Motion parallel to the field line with speed $v\cos(\alpha)$. (3) A third component is a motion perpendicular to the field line called the guiding-center drift. The predominant part of this drift is called the $\hat{E} \times \hat{B}$ drift, which in this case provides 'corotation', as if the magnetic field line it gyrated about rotated with Jupiter. This corotation drift actually lags slightly behind Jupiter's rotation, we used a value of 76 km s^{-1} (Kivelson et al., 2009). We also included the gradient-curvature drift (Thomsen and Van Allen, 1980). This was found to be much less important than the corotation $\hat{E} \times \hat{B}$ drift for the ions that sputter Europa's surface and so we will not discuss it further. This component of the drift is, however, important for the relativistic electrons that bombard Europa (Paranicas et al., 2009; Dalton et al., this issue). These are not discussed here because electrons have small sputtering yields compared to ions (see Section 2.3).

We assume that Jupiter's magnetic field, in the vicinity of the region we are simulating, is anti-parallel to Europa's spin axis, as in Pospieszalska and Johnson (1989). Jupiter's tilted dipole actually results in a time-varying, slightly tilted magnetic field at Europa's orbit, but Europa's interior conductivity (due to the presence of an ocean) cancels out the time-varying component of the field near Europa's surface, leaving just the anti-parallel component (Zimmer et al., 2000). Except for this consideration, we treat Europa as electromagnetically inert.

One difference between Pospieszalska and Johnson (1989) and the current model is that we trace the ions backward in time from Europa's surface. This is more computationally efficient in that we only calculate ion trajectories that intersect Europa's surface. The method works as follows: for a given location on Europa's surface, ion incidence direction and energy, the ion's motion is traced backward in time. If the ion's reverse motion intersects the sphere defining Europa's surface, then that trajectory is forbidden; ion flux to that location has been blocked by Europa's surface. If the ion travels sufficiently far 'upstream' of Europa, then that ion's trajectory is allowed and its flux is added to that location's total, the ion flux being defined by

$$(\vec{v} \cdot \hat{n}) df(E, \Omega) \Delta E \Delta \Omega \quad (1)$$

Where $f(E, \Omega) \Delta E \Delta \Omega$ is the ion energy and angular distribution measured near Europa's orbit, but far from Europa itself. It is also called the phase space density, and is described in the next section. This is multiplied by the energy and solid angle increments used by the program, d is the ion density, and $(\vec{v} \cdot \hat{n})$ is the ion speed relative to the surface dotted into the surface normal. This is another improvement over Pospieszalska and Johnson (1989), who did not quantify the flux, only bombardment patterns.

The description above is equivalent to employing Liouville's theorem, which states that the phase space density f is conserved along a dynamical trajectory. This is a rough approximation for Europa as f is known to change through mechanisms such as pitch angle scattering (Williams and Mauk, 1997). Another approximation is that we treat Europa as electromagnetically inert. However electrical currents induced in Europa's ionosphere divert plasma around Europa to an uncertain extent (Saur et al., 1998). Such diversion would have a small effect on the energetic ions, but could have dramatic effect on the 'cold' ions.

2.2. Plasma flux parameters

The phase space density $f(E, \Omega)$ and density d are given in several recent reviews. The distribution function is broken up into two different ion 'populations', reflecting the different instruments used to characterize the populations. The distribution function is a sum of these two populations. The 'cold' or 'thermal' population is described by Kivelson et al. (2009), it is composed of oxygen ($\sim 110 \text{ cm}^{-3}$) and sulfur ($\sim 20 \text{ cm}^{-3}$) and the energy distribution f is roughly a Maxwellian with temperature $\sim 100 \text{ eV}$. There is also a $\sim 20 \text{ eV}$ cold hydrogen population (Paterson et al., 1999).

The much more energetic population is described by Mauk et al. (2004) and Paranicas et al. (2009). We refer to this as the 'hot' population. The hot f is described by a power law extending from 50 keV to 50 MeV , with most of the flux coming from ion with energies less than 1 MeV . We used the parameters listed in Paranicas et al. (2009), Table 1 for H⁺, Oⁿ⁺, and Sⁿ⁺, calculating densities from the fluxes reported there. The densities for the hot

Guiding Center Motion:

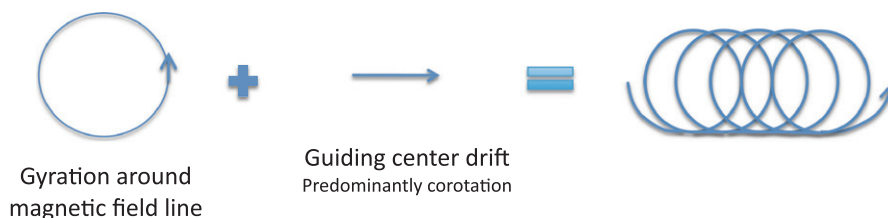


Fig. 1. Schematic of ion motion perpendicular to Jupiter's magnetic field line (pointing into the page). There is also motion parallel to the field.

Table 1

List of NIMS observation locations and estimated H₂O regolith grain sizes. The average ice grain size from the linear mixture model is listed first, followed by the output of the model. 14ENSUCOMP01 consists of multiple observations, so the model output is not given. In that case the solutions consisted almost entirely of 75 and 100 μ m grains. The non-ice portion of the surface consists of the various hydrates and a neutral dark absorber.

Observation	W. Longitude	Latitude	Grain Size	Symbol on Fig. 7
14ENSUCOMP01 (Shirley et al., 2010)	170°–185°	26°–29° South	85–100 μm	Plus Signs
14ENSUCOMP03 (Dalton et al., 2012)	203°	19.5° North	250 μm , 34 % 250 μm , 76 % non-ice	Circle
15ENSUCOMP01 Dalton et al. (2012)	114°	7.3° North	55 μm , 67% 50 μ m, 15% 75 μ m, 18 % non-ice	Asterisk
17ENSUCOMP02 Dalton et al. (2012)	120°	63° South	80 μm , 65% 75 μ m, 16% 100 μ m, 19 % non-ice	Triangle
G1ENNHLAT01 (this paper)	271°	13° North	930 μm , 2.5% 750 μ m, 6.3% 1000 μ m, 92 % non-ice	Diamond

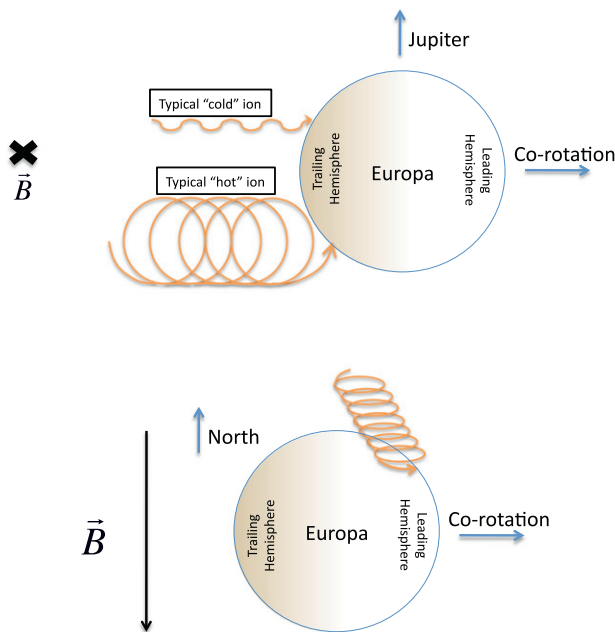


Fig. 2. (a) (top): Schematic of ion motion, looking down onto Europa's North pole. The gyroradius is to scale for a 1 MeV S⁺⁺ ion with a 30° pitch angle. (b) (bottom): Schematic of ion motion, looking from the side. This schematic demonstrates the importance of motion perpendicular to the field line. The slant of the ion motion is determined by its motion parallel to the magnetic field (vector at left) and the corotation drift (rightward) motion. Slant is not to scale.

population are much lower than the cold population, about 0.4 cm⁻³ for Sⁿ⁺, 0.2 cm⁻³ for Oⁿ⁺, and 0.1 cm⁻³ for H⁺. The angular portion of $f(E, \Omega)$ is known as the pitch angle distribution (PAD). We used isotropic PADs for both the hot and cold populations. Mauk et al. (2004) wrote that the hot population PAD in the vicinity of Europa's orbit is nearly uniform (to within 25%). As for the cold ions, the PAD does not matter. This population is so cold that its thermal speed does not affect the flux onto Europa's surface, only the drift speed matters (see Fig. 2).

Both of these populations exhibit some temporal variability. Kivelson et al. (2009) estimated that the cold ion density varies by a factor of two, and Paranicas et al. (2009) estimated that the hot ion flux also varies by about a factor of two.

The charge state of the ions is an important parameter as it helps to determine the gyroradius of the ions (Fig. 2, top). This is a poorly constrained quantity for the hot ions. Lagg et al. (2003) estimated that the oxygen and sulfur ions are multiply charged, but tend toward lower charge states over time by capturing electrons from neutral gas orbiting Jupiter. We chose a charge state of 2+ for the oxygen and 3+ sulfur ions, following Cooper et al. (2001) (and references therein). We do not expect the charge state to affect the sputtering yield; electrons are stripped from and captured by ions as they travel through a solid so that incident ions quickly lose their original charge state upon entering the surface.

As mentioned above, Jupiter's magnetic field is slightly tilted relative to Europa's orbit plane. As a result, Europa's plasma environment changes as the dipole spins. To account for this we used averaged plasma parameters. The parameters we just described apply to the 'centrifugal equator', the equilibrium surface at which the cold plasma density maximizes (at Europa's distance, it lies between the planet's magnetic equator and the rotational equator), but Europa moves above and below this plane by ~ 1 Jupiter radius (R_J). The cold plasma decreases in density as $\exp(-(z/H)^2)$ above the centrifugal equator with a scale height of $H \sim 1 R_J$ (Bagenal, 1994), resulting in an average cold ion density of 0.75 times the centrifugal value above. The hot ions do not decrease much in density above the centrifugal equator owing to their uniform PAD (Roederer, 1970).

2.3. Sputtering yields

Another quantity we need is the sputtering yield, the number of H₂O molecules ejected per incident ion (including other molecules produced during bombardment, mainly O₂ and H₂). The water ice sputtering yield is an experimentally determined quantity that has been fit with various functional forms, including dependencies on ion energy, ion mass, nuclear charge, water ice temperature and incident angle. We found that we needed two different functional forms to fit the available experimental data. One approximation from Famá et al. (2008) is appropriate for low (< 100 keV) energy ions. This is the upper limit for applicability specified in their paper. The other expression, from Johnson et al. (2009), matches the data above 100 keV. These two fits and available experimental data are shown in Fig. 3. Note that some sputtering yields from Fig. 3 were corrected for non-normal ion incidence and high temperature using the expressions from Famá et al. (2008).¹ This temperature dependence is important for Europa, we explicitly include this effect in our modeling with Eq. (2) below.

We included this temperature dependence in our calculated sputtering yield by estimating the surface temperature with a numerical thermal model (Spencer et al., 1989),² using the albedo and thermal inertia values from Spencer et al. (1999) as input. This was implemented by calculating, at each latitude, the diurnal average of the temperature factor mentioned above

$$Y(T) = Y(T=0)(1 + 220 \exp[-0.06 \text{ eV}/kT]) \quad (2)$$

where Y is the sputtering yield. The expressions above apply to the total sputtering yield, including all sputter products. A sputtering yield of 1 means that the given ion ejects, on average, the mass equivalent of one H₂O molecule, though some portion of the ejecta is actually O₂ and H₂ (more this below). This temperature enhancement factor is about 2 at Europa's subsolar point (~ 130 K) and about 1 on the nightside equator (~ 80 K).

¹ These expressions are not unique to Famá's paper, see, e.g., Johnson, 1990.

² Code is available here: <http://www.boulder.swri.edu/~spencer/thermprojrs/>.

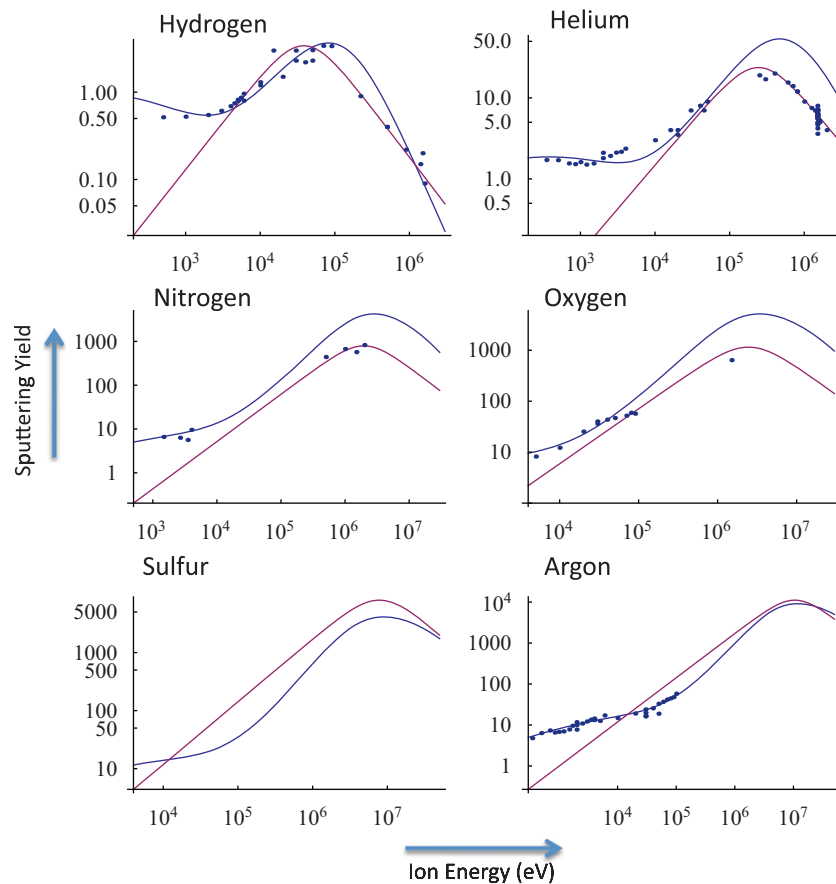


Fig. 3. Compilation of sputtering yield data and theory. Experimental data points best match the Fama et al. curve (blue) below ~ 100 keV and match the Johnson curve (red) above 100 keV. There are no available experimental results for sulfur ion sputtering, but the calculated sputtering yield is shown here because sulfur is the most important sputtering agent at Europa. The data were compiled from various experimental sputtering papers by R. E. Johnson and M. Liu at <http://people.virginia.edu/~rej/h2o.html>. Note that the cold ions hit Europa at ~ 500 eV (oxygen) or ~ 1000 eV (sulfur) while the hot ions have a wide range of energies (100s of keV to MeV). (For interpretation of the references to color in this figure legend, the reader is referred to the web version of this article.)

Europa's surface appears to be covered in a porous regolith (Domingue and Verbiscer, 1997), and this affects the sputtering yield. Most molecules sputtered from within a regolith actually hit other grains, rather than directly leaving the surface. This can lower the sputtering yield by around 75% if the sputter products 'stick' or freeze to the grains. At the same time the regolith enhances the sputtering yield as ions cross the almost randomly oriented grain surfaces with a variety of incidence angles, and non-normal incidences increase the sputtering yield (e.g., Johnson, 1990). The two effects largely cancel each other out, and we ignore them here (Cassidy and Johnson, 2005). The surfaces of regolith grains are themselves are not likely to be smooth at the atomic scale, but one computational study (Rodriguez-Nieva et al., 2011) suggested that nm scale porosity should not affect the sputtering yields.

Finally, the sputtering (ion erosion) rate is found by multiplying the calculated differential ion flux ($\text{cm}^{-2}\text{s}^{-1}\text{eV}^{-1}$) by the appropriate sputtering yield and integrating. As previously noted, photons and electrons also sputter water ice, but have much smaller sputtering yields, and so make only a small contribution to the sputtering rate (Cooper et al., 2001; Plainaki et al., 2010).

3. NIMS observations of H₂O ice grain sizes

Below we relate the sputtering rate with H₂O grain size. In this section we describe the observations and grain size derivation.

Shirley et al. (2010) and Dalton et al. (2012) provide detailed composition and H₂O grain size information for multiple widely spaced locations on Europa, based on an ongoing reanalysis of NIMS data. They have measured the cryogenic spectra of hydrated materials (e.g., $\text{H}_2\text{SO}_4 \cdot n\text{H}_2\text{O}$, $\text{Na}_2\text{SO}_4 \cdot n\text{H}_2\text{O}$) present on Europa's surface. They estimate Europa's surface composition with a spectral model that adds these reference spectra linearly, adjusting the composition until it finds the best match to the NIMS spectra.

The model only estimates regolith grain size for the pure water ice component of the surface, and so the grain size discussed here is for the water ice component of the surface only. The water ice reference spectra used for the mixture model were generated with a radiative transfer model for a discrete set of grain sizes between 25 and 5000 μm .

For the present study we employ the published data from Shirley et al. (2010) and Dalton et al. (2012) (Table 1 and Fig. 4). The observation footprints are shown in Figs. 4 and 7. We only use spectral solutions from a single kind of geological terrain to avoid comparison between areas of radically different composition or geological history. We chose the ridged plains as they have been exposed to Europa's radiation environment for the longest time, and their surface properties and compositions should reflect an equilibrium between endogenic and exogenic influences.

While it may appear that the number of data points employed for the study is small, it should be emphasized that each of the spectra employed was obtained by averaging of dozens to hundreds of carefully selected and processed individual NIMS spectra. These are optimal conditions for the preservation of the

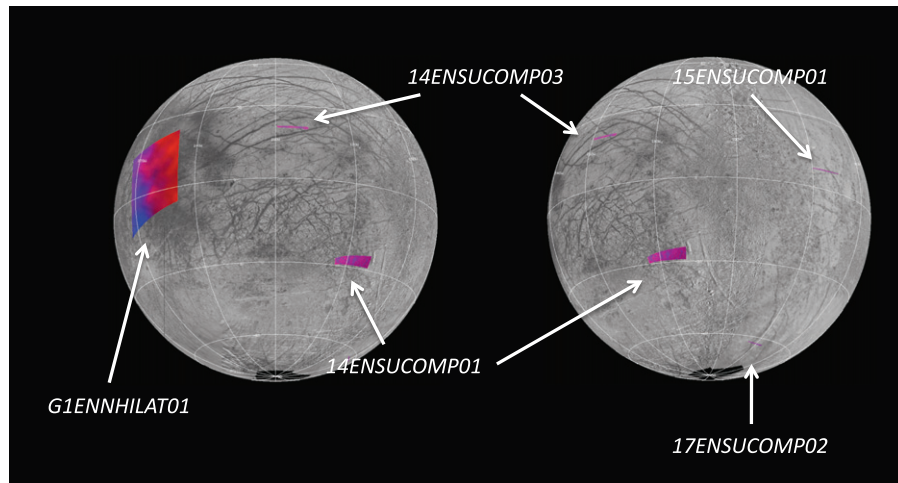


Fig. 4. Global image mosaic views of Europa with locations of the NIMS observations employed in this study. Left: Trailing hemisphere perspective Right: Leading hemisphere perspective.

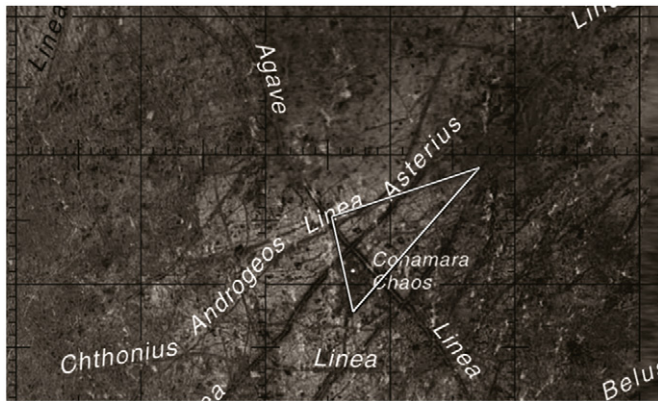


Fig. 5. Regional context image showing the source area (triangle) for the trailing hemisphere apex location analyzed here. The triangular selection area was chosen to avoid data drop-outs (due to incomplete wavelength coverage) that are present in the NIMS dataset. The area shown represents the northwestern corner of the G1ENNHILAT01 observation sub-area shown in Fig. 4. This study area was chosen because it exhibits a higher abundance of water ice than is found for adjacent areas to the south and east. The underlying basemap is available from the USGS Flagstaff Planetary Geologic Mapping website (<http://astrogeology.usgs.gov/Projects/PlanetaryMapping/>).

subtle signatures of the various ice grain sizes actually present on the surfaces imaged.

In this paper we describe new results (including water ice abundance and grain size) for a key location near Europa's trailing apex (observation G1ENNHILAT01 in Fig. 4). NIMS imaged a large portion of Europa's anti-Jovian hemisphere at moderate (38 km/pixel) resolution during the first orbital encounter (G1) of the Galileo Mission. The observation G1ENNHILAT01 spans latitudes from below the equator to the northern polar regions, with trailing side apex locations imaged at an oblique viewing angle near the western limb.

The previous studies in Table 1 had high enough resolution to permit the selection of ridged plains observations, whereas the trailing apex observation reported here covers a broad area and includes more than one kind of geological terrain. This exception is due to the lack of higher-resolution coverage, preventing the certain identification of geological terrain. A subsection of that trailing apex observation was selected for analysis here, shown in Fig. 5. It was chosen for its relatively high abundance of water ice compared to other areas in the observation. We extracted an area-average spectrum from the 66 NIMS pixels falling within the

area indicated on Fig. 5. This spectrum and the accompanying spectral model solution are shown in Fig. 6.

The area selected for analysis (Fig. 5) includes a portion of Conamara Chaos, a severely disrupted region characterized by large (several km) tilted and rotated ice blocks separated by rough hummocky matrix materials. The linear mixture model, however, only estimates grain size for the pure water ice component of the mixture, making it unlikely that this non-icy chaos terrain is influencing the grain size estimate.

The presence of relatively large-grained ice in the mixture model solution is a key result for the present investigation. Ice grains with 1 mm and 750 μm diameters are not seen in any of the other locations thus far analyzed (Dalton, 2007; Shirley et al., 2010; Dalton et al., 2012).

The 65% sulfuric acid hydrate abundance of Fig. 6 agrees well with the 62% abundance obtained by Dalton (2007), who employed an average spectrum for 18 contiguous visibly dark pixels from G1ENNHILAT01. No water ice was called for in the prior solution, which did not overlap with the area selection made here. The present solution shows moderate abundances of hexahydrite and epsomite, magnesium sulfate hydrates which are known to be quite stable under irradiation (McCord et al., 2001). In general, the high abundance of sulfuric acid hydrate, the presence of only the most stable of the hydrated salts, and the large grain sizes are all consistent with the expected effects of high levels of magnetospheric bombardment (Clark et al., 1983; Carlson et al., 1999; McCord et al., 2001; Dalton, 2007; Shirley et al., 2010; Dalton et al., 2012).

The accuracy of the grain size determinations is a complicated matter. The sensitivity of the linear mixture modeling algorithms to variations in water ice grain sizes is discussed in some detail in Appendix C of Shirley et al. (2010). There it was shown that single-step increases and decreases of water ice grain size give rise to diagnostic differences in the spectra, particularly near wavelengths of 2.05 and 2.25 μm . The mixture modeling algorithms are sensitive to these differences, returning significantly larger χ -squared values (indicating poorer fits) for cases where an incorrect grain size was artificially specified. While we are unable to rigorously quantify the error bars for the size determination, the algorithm is clearly capable of distinguishing between the spectra representing each of the grain size dimensions we have employed. Further, as also shown in the cited paper, abundance differences of $\geq 3\%$ of any component also yields noticeable degradation of the χ -squared values. Thus we believe a 3% error bar (1-sigma) is appropriate for the stated percent abundances of the single grain size components (50 μm , 75 μm , etc).

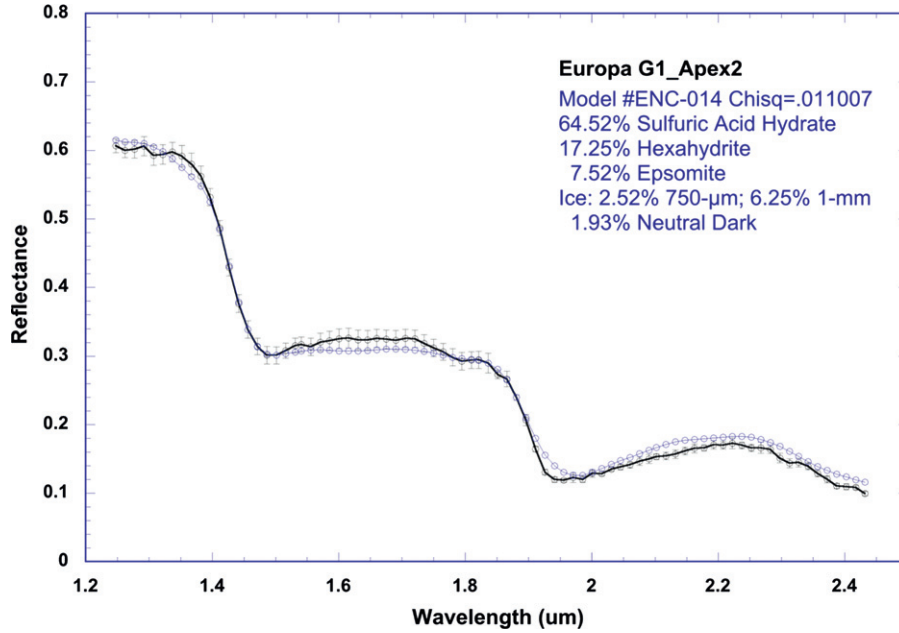


Fig. 6. Reflectance spectrum and linear mixture modeling results for Conamara Chaos and vicinity (Fig. 5). The extremely distorted water ice absorption bands at 1.5 and 2.0 μm are indicative of a high abundance of hydrated species (including hydrated sulfuric acid) in this location. $1-\sigma$ error bars are provided. (For interpretation of the references to color in this figure legend, the reader is referred to the web version of this article.)

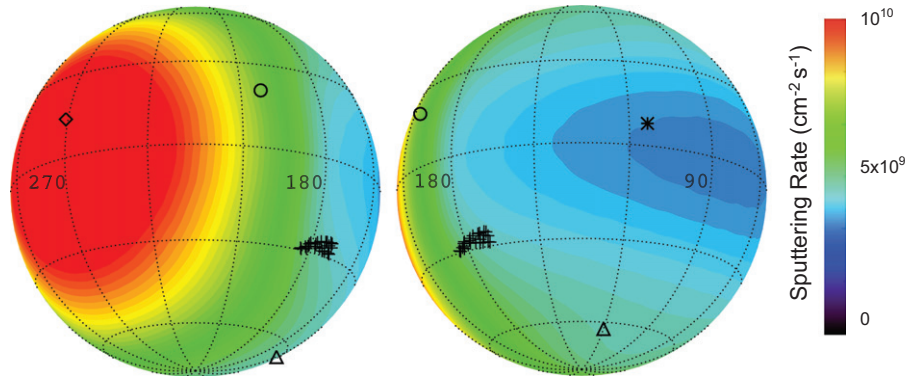


Fig. 7. Calculated sputtering (ion erosion) rate on Europa's surface. Symbols show approximate locations where NIMS data has been analyzed. Table 1 gives the estimated regolith grain sizes at these locations. Grain sizes and sputtering rates are shown in Fig. 10. Note on the right-hand side that the sputtering yield increases with latitude on the leading hemisphere. We will show below that this is principally an effect of the preferential bombardment of the polar regions by hot ions. (For interpretation of the references to color in this figure legend, the reader is referred to the web version of this article.)

While the difference between 25 and 50 μm grain sizes may not seem particularly important, one must at the same time recognize that one of these is twice as large as the other; for spectroscopic investigations, and considerations involving photon path lengths, this difference is both easily detectable and quite significant.

In reality the imaged surfaces must be expected to exhibit a continuum of ice grain sizes. We believe it is a strength of our method that reference spectra representing multiple grain sizes may be linearly combined in precise proportions to optimize the match between observed and model spectra. While the combinations we have obtained are not unique, we are unaware of any other technique that is capable of improving on the estimates presented here.

4. Results

4.1. Europa sputtering rates

Fig. 7 and Table 2 show the results of our ion tracing model calculations. Overall, there is about a factor of 3 difference between the peak sputtering rates at the leading apex (90°W

Longitude) and trailing apex (270°W Longitude). The largest sputtering agent, as measured by the global sputtering rate, is the hot sulfur ion population (Table 2), although cold oxygen is important right at the trailing apex. Fig. 7 also shows the locations where regolith grain sizes have been estimated using the Galileo NIMS observations.

The globally-averaged sputtering rate is $\sim 7 \times 10^9 \text{ cm}^{-2} \text{ s}^{-1}$. This number is similar to earlier estimates that assumed uniform ion flux. Cooper et al. (2001) estimated a factor of 4 lower sputtering rate while Paranicas et al. (2002), surprisingly, calculated an identical number. This sputtering rate corresponds to an erosion rate of 70 m per 10^9 years. Given that $\sim 1/3$ of sputtered H_2O is has enough energy to escape Europa's gravity, this corresponds to a loss of ~ 20 m per 10^9 years.

To better show the effect of ion energy on the sputtering map, Fig. 8 shows sulfur ion flux maps for a single energy ion population and a uniform PAD. At 10^2 eV, an energy typical of the cold population, sulfur ions have very small gyroradii and the ion speed (25 km s^{-1}) is small compared to the corotation drift speed (76 km s^{-1}). This situation is shown schematically in Fig. 2 (ion trajectory labeled 'cold'). The corotation drift carries the ions

Table 2

Sputtering rates and ion fluxes for each ion population. Note that the peak sputtering rate occurs on the trailing hemisphere apex (270°W), except for the hot hydrogen, where the peak sputtering rate is at the poles.

Species	Total sputtering rate	Total ion flux	Peak sputtering rate	O ₂ sputtering rate
Cold S ⁿ⁺	$8 \times 10^{25} \text{ s}^{-1}$	$9 \times 10^{24} \text{ s}^{-1}$	$1 \times 10^9 \text{ cm}^{-2} \text{ s}^{-1}$	$3 \times 10^{25} \text{ s}^{-1}$
Hot S ⁿ⁺	$1 \times 10^{27} \text{ s}^{-1}$	$1 \times 10^{24} \text{ s}^{-1}$	$4 \times 10^9 \text{ cm}^{-2} \text{ s}^{-1}$	$2 \times 10^{25} \text{ s}^{-1}$
Cold O ⁿ⁺	$3 \times 10^{26} \text{ s}^{-1}$	$4 \times 10^{25} \text{ s}^{-1}$	$4 \times 10^9 \text{ cm}^{-2} \text{ s}^{-1}$	$8 \times 10^{25} \text{ s}^{-1}$
Hot O ⁿ⁺	$2 \times 10^{26} \text{ s}^{-1}$	$6 \times 10^{23} \text{ s}^{-1}$	$8 \times 10^8 \text{ cm}^{-2} \text{ s}^{-1}$	$6 \times 10^{24} \text{ s}^{-1}$
Cold H ⁿ⁺	$9 \times 10^{23} \text{ s}^{-1}$	$1 \times 10^{24} \text{ s}^{-1}$	$1 \times 10^7 \text{ cm}^{-2} \text{ s}^{-1}$	$1 \times 10^{23} \text{ s}^{-1}$
Hot H ⁿ⁺	$3 \times 10^{24} \text{ s}^{-1}$	$2 \times 10^{24} \text{ s}^{-1}$	$2 \times 10^7 \text{ cm}^{-2} \text{ s}^{-1}$	$3 \times 10^{24} \text{ s}^{-1}$
Total	$2 \times 10^{27} \text{ s}^{-1}$			$1 \times 10^{26} \text{ s}^{-1}$

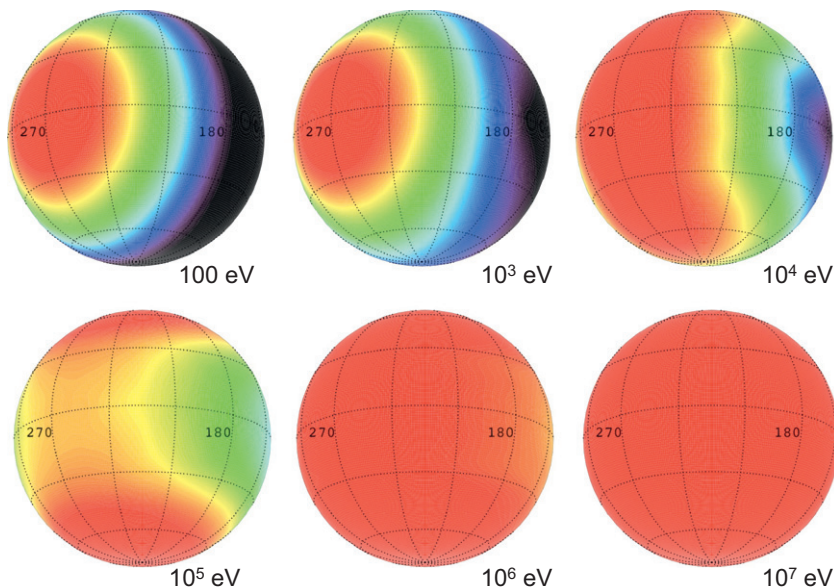


Fig. 8. S⁺⁺ flux patterns as a function of energy. Each map was produced by using a single energy ion energy with an isotropic pitch angle distribution. (For interpretation of the references to color in this figure legend, the reader is referred to the web version of this article.)

onto the trailing hemisphere, resulting in the bullseye pattern centered on the trailing apex (Fig. 8, upper left). This can be understood using Eq. (1), with $\dot{\nu}$ almost purely in the corotation direction, resulting in a $\cos(\theta)$ flux pattern, where θ is the angular distance from the trailing hemisphere apex.

Hendrix et al. (2011) focused on this cold population, reporting a similar bullseye pattern in the UV surface reflectance, which we attributed to absorption by SO₂ in the surface. That paper presented some of these results, with a focus on the sulfur ion flux, and we concluded that the bulls eye of cold sulfur ion flux is likely responsible for the SO₂ bulls eye. The hot sulfur, in comparison, has negligible flux, though those ions dominate the sputtering rate, as concluded by Paranicas et al. (2002) and Plainaki et al. (2010).

At 10³ eV, the ion speed becomes comparable to the corotation drift speed, though the gyroradii are still small compared to Europa's radius. At this energy the ion motion parallel to the magnetic field lines (oriented North/South) becomes important for reasons we now describe. With increasing ion speed the corotation drift remains unchanged³ and so the average ion speed in the corotation direction remains 76 km s⁻¹. The ion motion parallel to the magnetic field faces no such restriction though, and at high energies the ions increasingly reach Europa's surface from

the North or South. At 10⁵ eV (Fig. 8), the ion flux peaks at the poles. At even higher energies the gyroradius is comparable to Europa's radius and the ions can access Europa's surface from all directions, as seen in the nearly uniform flux of the 10⁶ eV case.

Most of the sputtering in our calculation is due to sulfur ions with energies on the order of 10⁵ eV, yet the corresponding map in Fig. 8 does not seem to correspond closely to the sputtering map in Fig. 7. There are two reasons for this: first, the temperature effect (Eq. (2)) enhances sputtering near the equator, offsetting the poles' advantage in energetic ion flux. Second, the cold ion population (mostly O⁺) results in a large sputtering rate near the trailing apex.

In contrast to the sputtering map, energetic H⁺ and electron flux peaks at the poles owing to their extremely small gyroradii and high speeds (Truscott et al., 2010; see companion paper by Dalton et al. (2012) in this issue).

4.2. O₂ sputtering rate

As ions and electrons erode the surface, ejecting H₂O molecules, they also create H₂, O₂ and other species in a process called radiolysis. O₂ created by radiolysis, then subsequently sputtered or thermally desorbed from the surface, forms the dominant component of Europa's tenuous atmosphere (Johnson et al., 1982; Hall et al., 1998). Here we provide the first estimated map of its source rate.

³ The gradient curvature drift also changes with ion energy, but it is small compared to the corotation drift for the ions considered here.

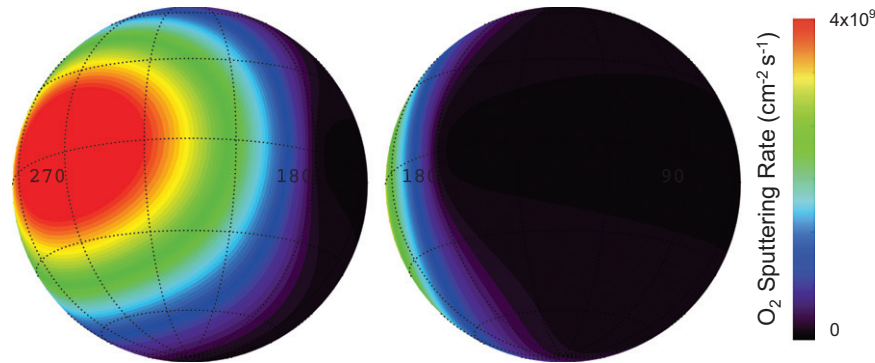


Fig. 9. Calculated O_2 sputtering rate on Europa's surface. Note that unlike the total sputtering rate (Fig. 7), the O_2 sputtering rate is mostly confined to the trailing hemisphere.

The sputtering yields described above are the *total* sputtering yields, in this section we examine the H_2 and O_2 portion. Teolis et al. (2010) used published laboratory data to develop an empirical model of O_2 production. We used their yields to estimate the O_2 production on Europa's surface. By stoichiometry, the H_2 production rate is exactly twice that of the O_2 sputtering rate. This is the first such estimate of O_2 and H_2 production. Estimates of these sputtering rates usually assume that the O_2/H_2 portion of the yield is some fixed fraction of the H_2O sputtering rate (see, e.g., Saur et al., 1998 and Smyth and Marconi, 2006). In contrast our O_2/H_2 fraction depends on projectile, energy and surface temperature.

Fig. 8 and Table 2 show the O_2 sputtering rate. Unlike the total sputtering rate (Fig. 7), the O_2 is created almost entirely on the trailing hemisphere. This is because low-energy heavy ions (like oxygen), which bombard the trailing hemisphere in a bullseye pattern, are effective at producing O_2 . In contrast, the hot ions dominate the overall sputtering yield owing to their huge advantage in sputtering yield. Energetic ions still have larger O_2 yields, but not the two-order of magnitude advantage seen in Fig. 3. Teolis et al. (2010) explained why cold ions have high O_2 sputtering yields. Radiolytic production is often parameterized by a quantity called the 'G value', the number of molecules created per unit energy deposited in a surface by ions or electrons. The G value for O_2 production varies by over 4 orders of magnitude, but Teolis et al. found that they could parameterize the available data with a single depth-dependent G value, with the G value decreasing rapidly with depth. Teolis et al. (2005) had previously found that O_2 is produced in the top few nm near the ice surface even by ions that penetrate much further.

Low-energy heavy ions (like our 'cold' S^{n+} and O^{n+}) do not penetrate deeply into the ice and so deposit most of their energy near the surface unlike more penetrating energetic ions, such as the 'hot' sulfur ions responsible for most of the H_2O sputtering.

Like the total yield, the O_2 yield also has temperature dependence. Based on measurements of O_2 sputtering yields at various temperatures the temperature dependence is given by

$$Y(T) = Y(T=0)(1 + 1000 \exp[-0.06 \text{ eV}/kT])$$

which is similar to the temperature dependence of the total sputtering yield (Eq. (2)), but more sensitive to temperature (the only difference is the factor of 1000 replacing 220). This temperature dependence would result in a factor of ~ 5 difference in O_2 production between night and day, except that Teolis et al. (2005) found that the O_2 yields have a delayed response to changes in temperature. They found that it takes a flux of about 1×10^{15} ions cm^{-2} , deposited over any length of time, before the yield adjusts. At Europa's trailing apex that corresponds to about 15 European days. For that reason we used the diurnally-averaged O_2 sputtering yield.

The H_2O sputtering rate is actually nearly independent of temperature at the relevant temperatures (~ 80 – 130 K), the temperature dependence in the total sputtering yield (Eq. (2)) arises mostly from production and sputtering of O_2 and H_2 (Famá et al., 2008).

Overall, O_2 and H_2 sputtering are a minor component of the total sputtering rate ($\sim 10\%$ by mass). O_2 is the dominant species of the atmosphere, however, because it does not freeze to the surface like H_2O . H_2 is also abundant in the atmosphere, but it quickly escapes Europa's gravity. Assuming the atmosphere has the same temperature as Europa's surface, the O_2 is gravitationally bound but the H_2 is not (Smyth and Marconi, 2006).

There have been few observations of the O_2 atmosphere, which is detected via UV emission triggered by electron impact. Hansen et al. (2005) observed these emissions during Cassini's Jupiter flyby and found that the trailing hemisphere was much brighter than the leading hemisphere, in seeming agreement with Fig. 9. Further, occultations of Europa's ionosphere found it absent near the leading apex (Kliore et al., 1997). However, HST observations did not see the same leading/trailing asymmetry (Hall et al., 1998). Further, an asymmetric source of O_2 will not necessarily result in an asymmetric atmosphere. Cassidy et al. (2007) found that the O_2 spreads over Europa's surface during its short lifetime. Relating the O_2 source rate to these observations requires treatment of the exciting electrons, and thus treatment of the magnetosphere/moon interaction (e.g., Saur et al., 1998).

H_2 is produced along with the O_2 and at twice the rate, $2 \times 10^{26} \text{ s}^{-1}$. Assuming the H_2 has the same temperature as Europa's surface, it quickly escapes Europa's gravity to populate a 'cloud' or 'torus' at Europa's orbit. Such a cloud was inferred by Mauk et al. and Lagg et al. (2003), who could not definitively identify the species responsible. Smyth and Marconi (2006) concluded that H_2 from Europa is likely responsible (the other possibility being atomic O from Europa's O_2 atmosphere). They were not able to make a careful estimate of the H_2 sputtering rate, but used a value about 10 times larger than we report here, $1.9 \times 10^{27} \text{ s}^{-1}$.

4.3. Comparison of regolith grain size and sputtering rate

Clark et al. (1983) concluded that regolith grain sizes on the icy Galilean satellites (i.e., not including Io) are controlled by the sputtering rate, with larger sputtering rates producing larger grains. Though all grains are eroded at the same rate (per unit area), small grains lose mass faster than large grains due to their larger surface to volume ratio. That mechanism does not create large grains, simply destroys the smaller ones. In addition to destroying small grains, the sputtering may also help to grow large grains as water molecules may be more likely to adsorb onto

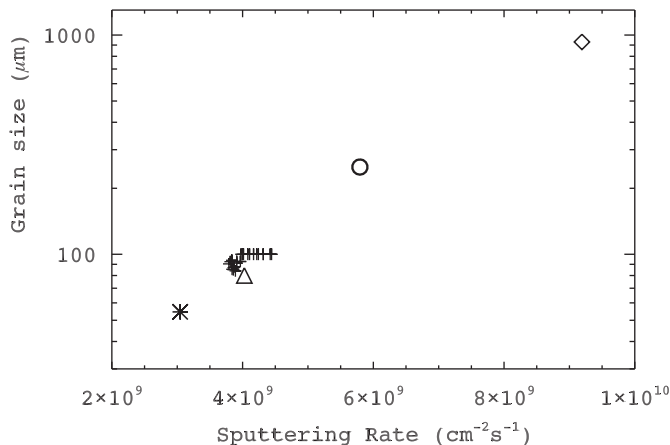


Fig. 10. Correlation between calculated sputtering rate and estimated grain size.

large grains, known to happen experimentally when the eroding agent is evaporation (Clark et al., 1983).

We test the idea that sputtering results in larger grains by looking at the correlation between our calculated sputtering rates and observed H₂O ice grain size. The observations and grain sizes are summarized in Table 1. These same locations are marked on the sputtering map in Fig. 7.

Fig. 10 shows the correlation between sputtering rate and mean grain size from Table 1. The Pearson correlation coefficient is 0.97. While the existence of a relationship linking H₂O ice grain size with sputtering rate is strongly suggested, correlation does not demonstrate causation. Caution is advisable, as our physical description of potentially relevant factors is clearly incomplete; we have not modeled all processes that might contribute to grain growth.

Another possibility is that some other exogenic process is responsible for the trend. Interplanetary impactors, for example, are expected to hit the leading hemisphere at much larger rates (Zahnle et al., 1998), and so might explain the small grain sizes found on the leading hemisphere. However such a process would be unlikely to explain the nearly identical grain sizes at the widely separated leading hemisphere observation points (indicated by the asterisk, triangle, and plus signs) along with a strong trend on the trailing hemisphere (circle, diamond).

The apparently minor difference in mean water ice grain sizes found for the leading side polar (triangle, 80 μm) and leading side apex (asterisk, 55 μm) locations may be explained by the difference in sputtering rates obtained for the two locations (note once again the higher sputtering rate shown for south polar regions in Fig. 7).

The data point for G1ENNHILO1 (diamond) corresponds to a different type of terrain (chaos rather than ridged plains). It is thus possible that the agreement of this point with the general trend is fortuitous. However, if we remove this point from the sample, the correlation remains high at 0.96. Perhaps the most that we can say is that the selection of large-grained ice for this location by the linear mixture model algorithms is a robust result that appears consistent with the trend established by the bright plains observations.

5. Discussion

Our investigation has uncovered a relationship linking the sputtering rate at Europa with the distribution of water ice grain sizes found at widely-spaced locations. Our physical parameterization of all potentially relevant processes affecting surface

water ice grain sizes is necessarily incomplete, and more work remains to be done. The present results nonetheless contribute to an improved understanding of the exogenic influences on Europa's surface properties and composition. It will be of interest to see how well the correlation holds up in the future, as additional NIMS observations at diverse locations are analyzed.

Sputtering represents only one of several important exogenic influences on Europa. In a companion paper (Dalton et al. (2012), this issue) we explore the energy deposition into Europa's surface as a function of location due to both energetic ions and to electrons. The interplay of sputtering, energy deposition, endogenic chemistry, and implanted exogenic species makes the study of Europa's surface properties and surface chemistry both challenging and rewarding.

6. Conclusion

We performed the first spatially-dependent calculation of Europa's sputtering rate using up-to-date plasma parameters and sputtering yields. We conclude, as others have previously, that hot sulfur ions are responsible for the majority of the sputtering. We performed the first detailed estimate of the O₂ and H₂ sputtering yields and found that cold heavy ions (sulfur and oxygen) are responsible for most of the O₂ and H₂ production. O₂ and H₂ are a minor component of the total sputtering rate (~20% by mass), but of the order of magnitude necessary to explain the observed O₂ atmosphere and H₂ torus.

We found that the connection between ion flux and sputtering rate is complicated. Though most of the sputtering is done by energetic sulfur ions whose flux peaks at the poles, the overall sputtering map shows the long-assumed leading/trailing asymmetry (e.g., Tiscareno and Geissler, 2003), with the sputtering rate peaked on the trailing apex. One finding from our approach is that cold oxygen can be competitive with energetic heavy ions in sputtering Europa's surface on the trailing hemisphere.

We found that experimental sputtering data is best fit by a combination of two analytic sputtering formulas. Below ~10⁵ eV, the formula from Famá et al. (2008) best fits the data. Above ~10⁵ eV the formula from Johnson et al. (2009) best fits the data. We reported new spectral fits to NIMS observations of the trailing hemisphere apex. The estimated surface composition shows a strong magnetospheric influence, including high concentration of sulfuric acid hydrate and radiation-resistant hydrated salts. We concluded that the sputtering rate is highly correlated with regolith grain size as suggested by Clark et al. (1983), but did not quantify the processes responsible. The NIMS observations and fits are described by Dalton et al. (2012) (this issue) in more detail.

Acknowledgments

TAC would like to thank Michael Kokorowski for useful discussions and for pointing out the Roederer (1970) reference. TAC and REJ thank Min Liu, at the University of Virginia, for help in compiling the sputtering yield data. Part of this research was carried out at the Jet Propulsion Laboratory, California Institute of Technology, under a contract with the National Aeronautics and Space Administration.

References

- Bagenal, F., 1994. Empirical model of the IO plasma torus: voyager measurements. *Journal of Geophysical Research* 99, 11043–11062.
- Carlson, R.W., Johnson, R.E., Anderson, M.S., 1999. Sulfuric acid on Europa and the radiolytic sulfur cycle. *Science* 286, 97–99.

- Cassidy, T.A., Johnson, R.E., 2005. Monte Carlo model of sputtering and other ejection processes within a regolith. *Icarus* 176, 499–507.
- Cassidy, T.A., Johnson, R.E., Geissler, P.E., Leblanc, F., 2008. Simulation of Na D emission near Europa during eclipse. *Journal of Geophysical Research* 113, E02005.
- Cassidy, T.A., Johnson, R.E., McGrath, M.A., Wong, M.C., Cooper, J.F., 2007. The spatial morphology of Europa's near-surface O₂ atmosphere. *Icarus* 191, 755–764.
- Clark, R.N., Fanale, F.P., Zent, A.P., 1983. Frost grain size metamorphism: implications for remote sensing of planetary surfaces. *Icarus* 56, 233–245.
- Cooper, J.F., Johnson, R.E., Mauk, B.H., Garrett, H.B., Gehrels, N., 2001. Energetic ion and electron irradiation of the icy galilean satellites. *Icarus* 149, 133–159.
- Dalton III, J.B., Shirley, J.H., Cassidy, T.A., Paranicas, C.P., 2012. Exogenic and endogenic controls on the radiolytic sulfur cycle at Europa. *Planetary and Space Science*.
- Dalton, J.B., 2007. Linear mixture modeling of Europa's non-ice material based on cryogenic laboratory spectroscopy. *Geophysical Research Letters* 34, L21205.
- Domingue, D.L., Verbiscer, A., 1997. Re-analysis of the solar phase curves of the icy Galilean satellites. *Icarus* 128, 49–74.
- Famá, M., Shi, J., Baragiola, R.A., 2008. Sputtering of ice by low-energy ions. *Surface Science* 602, 156–161.
- Hall, D.T., Feldman, P.D., McGrath, M.A., Strobel, D.F., 1998. The far-ultraviolet oxygen airglow of Europa and Ganymede. *The Astrophysical Journal* 499, 475.
- Hansen, C.J., Shemansky, D.E., Hendrix, A.R., 2005. Cassini UVIS observations of Europa's oxygen atmosphere and torus. *Icarus* 176, 305–315.
- Hendrix, A.R., Cassidy, T.A., Johnson, R.E., Paranicas, C., Carlson, R.W., 2011. Europa's disk-resolved ultraviolet spectra: relationships with plasma flux and surface terrains. *Icarus* 212, 736–743.
- Roederer, J.G., 1970. *Dynamics of Geomagnetically Trapped Radiation*. Springer-Verlag, New York.
- Johnson, R.E., Burger, M.H., Cassidy, T.A., Leblanc, F., Marconi, M., Smyth, W.H., 2009. Composition and Detection of Europa's Sputter-Induced Atmosphere. In: Pappalardo, R.T., McKinnon, W.B., Khurana, K.K. (Eds.), *Europa*. University of Arizona Press, Tucson.
- Johnson, R.E., Lanzerotti, L.J., Brown, W.L., 1982. Planetary applications of ion induced erosion of condensed-gas frosts. *Nuclear Instruments and Methods in Physics Research* 198, 147–157.
- Kivelson, M.G., Khurana, K.K., Volwerk, M., 2009. Europa's Interaction with the Jovian Magnetosphere. In: Pappalardo, R.T., McKinnon, W.B., Khurana, K.K. (Eds.), *Europa*. University of Arizona Press, Tucson.
- Lagg, A., Krupp, N., Woch, J., Williams, D.J., 2003. In-situ observations of a neutral gas torus at Europa. *Geophysical Research Letters* 30, 1556.
- Mauk, B.H., Mitchell, D.G., McEntire, R.W., Paranicas, C.P., Roelof, E.C., Williams, D.J., Krimigis, S.M., Lagg, A., 2004. Energetic ion characteristics and neutral gas interactions in Jupiter's magnetosphere. *Journal of Geophysical Research* 109, A09S12.
- McCord, T.B., Orlando, T.M., Teeter, G., Hansen, G.B., Sieger, M.T., Petrik, N.G., Van Keulen, L., 2001. Thermal and radiation stability of the hydrated salt minerals epsomite, mirabilite, and natron under Europa environmental conditions. *Journal of Geophysical Research* 106, 3311–3319.
- Paranicas, C., Cooper, J.F., Garrett, H.B., Johnson, R.E., Sturmer, S.J., 2009. Europa's Radiation Environment and Its Effects on the Surface. In: Pappalardo, R.T., McKinnon, K.K., Khurana, K.K. (Eds.), *Europa*. University of Arizona Press, Tucson.
- Paranicas, C., Ratliff, J.M., Mauk, B.H., Cohen, C., Johnson, R.E., 2002. The ion environment near Europa and its role in surface energetics. *Geophysical Research Letters* 29, 1074.
- Plainaki, C., Milillo, A., Mura, A., Orsini, S., Cassidy, T., 2010. Neutral particle release from Europa's surface. *Icarus* 210, 385–395.
- Pospieszalska, M.K., Johnson, R.E., 1989. Magnetospheric ion bombardment profiles of satellites: Europa and Dione. *Icarus* 78, 1–13.
- Johnson, R. E., 1990. *Energetic Charged-Particle Interactions with Atmospheres and Surfaces*.
- Rodriguez-Nieva, J.F., Bringa, E.M., Cassidy, T.A., Johnson, R.E., Caro, A., Fama, M., Loeffler, M.J., Baragiola, R.A., Farkas, D., 2011. Sputtering from a Porous material by penetrating ions. *The Astrophysical Journal Letters* 743, L5.
- Saur, J., Strobel, D.F., Neubauer, F.M., 1998. Interaction of the Jovian magnetosphere with Europa: Constraints on the neutral atmosphere. *Journal of Geophysical Research* 103, 19947–19962.
- Shirley, J.H., Dalton III, J.B., Prockter, L.M., Kamp, L.W., 2010. Europa's ridged plains and smooth low albedo plains: distinctive compositions and compositional gradients at the leading side–trailing side boundary. *Icarus* 210, 358–384.
- Smyth, W.H., Marconi, M.L., 2006. Europa's atmosphere, gas tori, and magnetospheric implications. *Icarus* 181, 510–526.
- Spencer, J.R., Lebofsky, L.A., Sykes, M.V., 1989. Systematic biases in radiometric diameter determinations. *Icarus* 78, 337–354.
- Spencer, J.R., Tappari, L.K., Martin, T.Z., Travis, L.D., 1999. Temperatures on Europa from Galileo photopolarimeter-radiometer: nighttime thermal anomalies. *Science (New York, NY)* 284, 1514–1516.
- Teolis, B.D., Jones, G.H., Miles, P.F., Tokar, R.L., Magee, B.A., Waite, J.H., Roussos, E., Young, D.T., Cray, F.J., Coates, A.J., Johnson, R.E., Tseng, W.-L., Baragiola, R.A., 2010. Cassini finds an oxygen–carbon dioxide atmosphere at Saturn's icy moon rhea. *Science (New York, NY)* 330, 1813–1815.
- Teolis, B.D., Vidal, R.A., Shi, J., Baragiola, R.A., 2005. Mechanisms of O₂ sputtering from water ice by keV ions. *Physical Review B* 72, 245422.
- Thomsen, M.F., Van Allen, J.A., 1980. Motion of Trapped electrons and protons in Saturn's inner magnetosphere. *Journal of Geophysical Research* 85, 5831–5834.
- Tiscareno, M.S., Geissler, P.E., 2003. Can redistribution of material by sputtering explain the hemispheric dichotomy of Europa? *Icarus* 161, 90–101.
- Truscott, P., Heynderickx, D., Nartallo, R., Lei, F., Sicard-Piet, A., 2010. Application of PLANETOCOSMICS to Simulate the Radiation Environment at the Galilean Moons. Presentation at the European Planetary Space Conference.
- Paterson, W.R., Frank, L.A., Ackerson, K.L., 1999. Galileo plasma observations at Europa: ion energy spectra and moments. *Journal of Geophysical Research* 104, 22779–22792.
- Williams, D.J., Mauk, B., 1997. Pitch angle diffusion at Jupiter's moon Ganymede. *Journal of Geophysical Research* 102, 24283–24287.
- Zahnle, K., Dones, L., Levison, H.F., 1998. Cratering Rates on the Galilean Satellites. *Icarus* 136, 202–222.
- Zimmer, C., Khurana, K.K., Kivelson, M.G., 2000. Subsurface oceans on Europa and Callisto: constraints from Galileo magnetometer observations. *Icarus* 147, 329–347.